Research Square

Preprints are preliminary reports that have not undergone peer review.
They should not be considered conclusive, used to inform clinical practice,
or referenced by the media as validated information.

Visual “Dam-Break Drainage” Nucleic Acid Chips: Family-Affordable Platform for Rapid and Ultrasensitive Pathogens Detection

Yang Sun

yangsunbio@ustb.edu.cn

University of Science and Technology Beijing

Kai Liu

University of Science and Technology Beijing

Xiang Li

University of Science and Technology Beijing

Meng Zhao

University of Science and Technology Beijing

Zhuo Yang

Shenyang Pharmaceutical University

Jingshuai Wen

University of Science and Technology Beijing

Jinpeng Liu

University of Science and Technology Beijing

Haoli Zhang

University of Science and Technology Beijing

Yuecan Zhao

University of Science and Technology Beijing

Zhengping Li

University of Science and Technology Beijing

Article

Keywords:

Posted Date: January 19th, 2026

DOI: https://doi.org/10.21203/rs.3.rs-8576721/v1

License: This work is licensed under a Creative Commons Attribution 4.0 International License.
Read Full License

Additional Declarations: There is **NO** Competing Interest.

Version of Record: A version of this preprint was published at Nature Communications on August 22nd, 2026. See the published version at https://doi.org/10.1038/s41467-026-77042-w.

Visual “Dam-Break Drainage” Nucleic Acid Chips: Family-Affordable Platform for Rapid and Ultrasensitive Pathogens Detection

Kai Liu[1]†, Xiang Li[1]†, Meng Zhao[1], Zhuo Yang[1], Jingshuai Wen[1], Jinpeng Liu[1], Haoli Zhang[1], Yuecan Zhao[1], Yang Sun[1*], Zhengping Li[1*]

[1] Beijing Key Laboratory for Bioengineering and Sensing Technology, School of Chemistry and Biological Engineering, University of Science and Technology Beijing, 30 Xueyuan Road, Haidian District, Beijing, 100083, PR China.

†These authors contributed equally to this work

*Corresponding author. Email: lzpbd@ustb.edu.cn

Abstract: The critical need for highly sensitive, rapid, low-cost and equipment-free pathogens diagnostics is acutely felt in resource-limited settings, such as in low-income region and at home, where existing methods force a compromise among these key metrics. We break this trade-off with a nucleic acid chip that leverages a novel “dam-break drainage” readout model and a CRISPR-Cas13a-mediated interfacial wettability switching sensing mechanism. This design unlocks both single-plex and duplex visual detection, delivering attomolar sensitivity (10 and 100 aM), rapid results (2 and 5 min) and low cost (0.20$ and 0.30$ per test), respectively. In a 40 clinical-samples validation for SARS-CoV-2, Influenza A virus and Influenza B virus, our platform demonstrated robust clinical concordance and successfully detected samples with ambiguous RT-PCR results (Ct=35). This work provides a powerful and accessible solution for next-generation point-of-care molecular testing.

Introduction

Infectious pathogens have persisted throughout human history, continuously posing serious threats to public health and social stability[1, 2]. Some pathogens display periodic outbreaks—such as Influenza A (IAV) and B (IBV) viruses—that cause seasonal epidemics and significant healthcare burdens[3]. Meanwhile, newly emerging and highly pathogenic agents have repeatedly triggered sudden global health crises, including severe acute respiratory syndrome (SARS), Middle East respiratory syndrome (MERS), Ebola virus disease, coronavirus disease 2019 (COVID-19) and more recently, chikungunya virus (CHIKV) outbreaks[4-9]. These events highlight that the threat of infectious diseases is not incidental but an enduring challenge. Consequently, the development of affordable, rapid, accurate and easily deployable diagnostic technologies is seriously needed for infectious disease prevention and control-particularly in resource-limited and low-income regions where such capabilities hold irreplaceable strategic value.

The COVID-19 pandemic has highlighted a persistent gap in diagnostic capabilities—lacking technologies that can simultaneously perform highly sensitivity, low cost, rapid turnaround and operational simplicity without reliance on specialized equipment[10]. Lateral flow immunoassays (LFAs)[11] offer simple, low-cost, rapid and instrument-free operation, yet their limited sensitivity restricts their use for early-stage pathogen screening. In contrast, nucleic acid amplification techniques represented by reverse transcription-polymerase chain reaction (RT-PCR) provide high sensitivity and flexible probe redesign for emerging variants[12], but require sophisticated temperature-control instruments, trained personnel and long assay times, making them unsuitable for low-cost, field-deployable and rapid testing. Alternative approaches based on SHERLOCK[13], DETECTR[14, 15], electrochemical[16, 17], colorimetric[18, 19] and optical signal transduction[20, 21] have further diversified the detection landscape, yet most still depend on nucleic acid pre-amplification or external readout instruments. Consequently, achieving high sensitivity, family-affordability, operational simplicity and rapidity within a single diagnostic platform remains a formidable challenge.

Here, we reported a breakthrough sensing paradigm—converting target recognition into a visible "dam-break drainage" readout through a programmable interfacial wettability switch mediated by CRISPR-Cas13a system. Based on this paradigm, we developed a diagnostic chip architecture comprising a sample reservoir, a functional dam, a microfluidic channel and a collection zone. In the absence of the target, liquid is confined in the sample reservoir by the dam structure; upon target recognition, the solution breaches the dam and flows into the channel, enabling unambiguous signal interpretation. This architecture is further engineered as a single-plex chip for individual pathogen detection and a duplex chip for simultaneous identification of two distinct targets. Using SARS-CoV-2 as a model, the single-plex chip achieved a detection limit of 10 aM within 2 min, at a cost of less than $0.20 per test. The duplex chip, demonstrated by simultaneous detection of Influenza A and B viruses, attained sensitivity of 100 aM for both targets within 5 min, costing under $0.30 per test. Clinical validation using 40 nasal swab samples (including SARS-CoV-2, IAV and IBV) showed 100% concordance with RT-PCR results. Notably, the platform reliably detected positives even at high cycle thresholds (Ct=35), where conventional assays often fail. These results collectively highlight the developed chips as a highly sensitive, rapid, low-cost and equipment-free platform for pathogen screening, particularly suited for low-resource settings.

Results

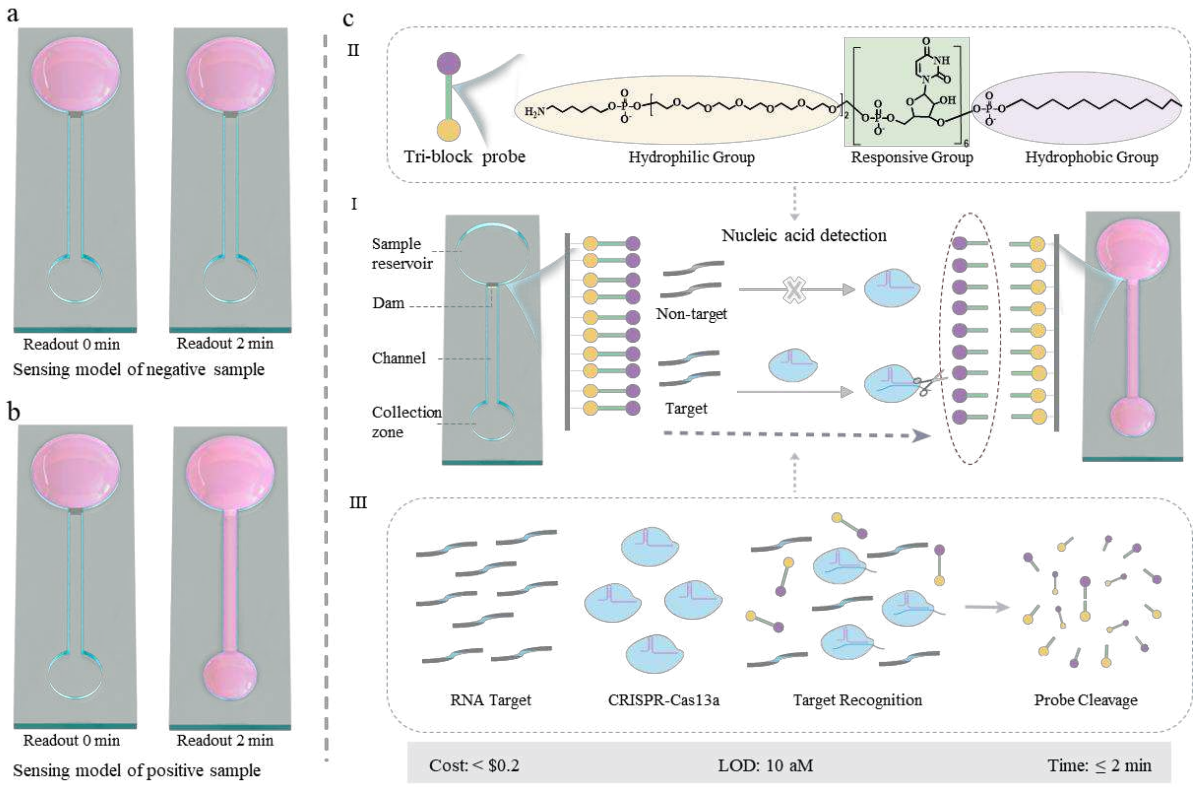


Figure 1 | Working flow of the single-plex chip. (a) Signal readout for the negative sample: the test liquid is retained in the sample reservoir after a 2 min incubation. **(b)** Signal readout for the positive sample: the liquid breaches the hydrophobic dam and undergoes a "dam-break drainage" phenomenon within 2 min. **(c)** Chip structure and sensing pathway of the single-plex chip **(cI)**; Architecture of the tri-block probe, consisting of a proximal hydrophilic moiety, a central responsive segment and a distal hydrophobic tail **(cII)**. Mechanism of target RNA-induced tri-block probe cleavage by CRISPR-Cas13a mediation **(cIII).**

Architecture and working principle of the single-plex chip. As shown in Fig. 1, the developed single-plex chip is capable of instrument-free, visual nucleic acid detection of pathogens at a cost below $0.2, with a limit of detection down to 10 aM and a total assay time of less than 2 min. The detection model of the chip operates as follows: when the sample is negative, the liquid is confined within the sample reservoir (Fig. 1a); When the sample is positive, the liquid breaches the dam and flows along the channel (Fig. 1b). To achieve this behavior, the chip was structurally divided into four functional zones-sample reservoir, dam, channel and collection zone (Fig. 1cI). At the dam region, we immobilized a tri-block probe composed of a hydrophilic group at the proximal end, a responsive linker in the middle and a hydrophobic tail at the distal end (Fig. 1cII). The immobilized tri-block probes render the overall dam surface hydrophobic, thereby preventing the liquid from flowing beyond the sample reservoir. We employed the CRISPR-Cas13a system as a target-activated mediator to degrade the responsive linker and trigger a hydrophobic-to-hydrophilic dam wettability transition. Owing to the programmability of crRNA, Cas13a′s RNase activity can be specifically activated by the target nucleic acid of any pathogen and a single activated Cas13a is able to cleave thousands of single-stranded RNA (ssRNA) substrates[22-24] (Fig. 1cIII). Accordingly, we designed the responsive linker as a ssRNA consisting of six uridine residues (6U), while the proximal hydrophilic group was formed by two PEG_6 chains and the distal hydrophobic group featured a $C_{12}H_{25}$ tail (Fig. 1cII). As shown in Fig. 1cI,

upon target recognition, the CRISPR-Cas13a system mediates efficient degradation of the ssRNA linker, resulting in a pronounced hydrophobic-to-hydrophilic wettability transition at dam surface. This transition allows the liquid to breach the dam and flow along the channel, producing a "dam-break drainage" phenomenon. Conversely, in the absence of target nucleic acid, the Cas13a protein remains inactive, preserving the integrity of the tri-block probe and preventing liquid flow. By integrating the sensing mechanism that CRISPR-Cas13a-mediated dam wettability switching with a "dam-break drainage" sensing model, this work opens a new window for point-of-care diagnostic solution.

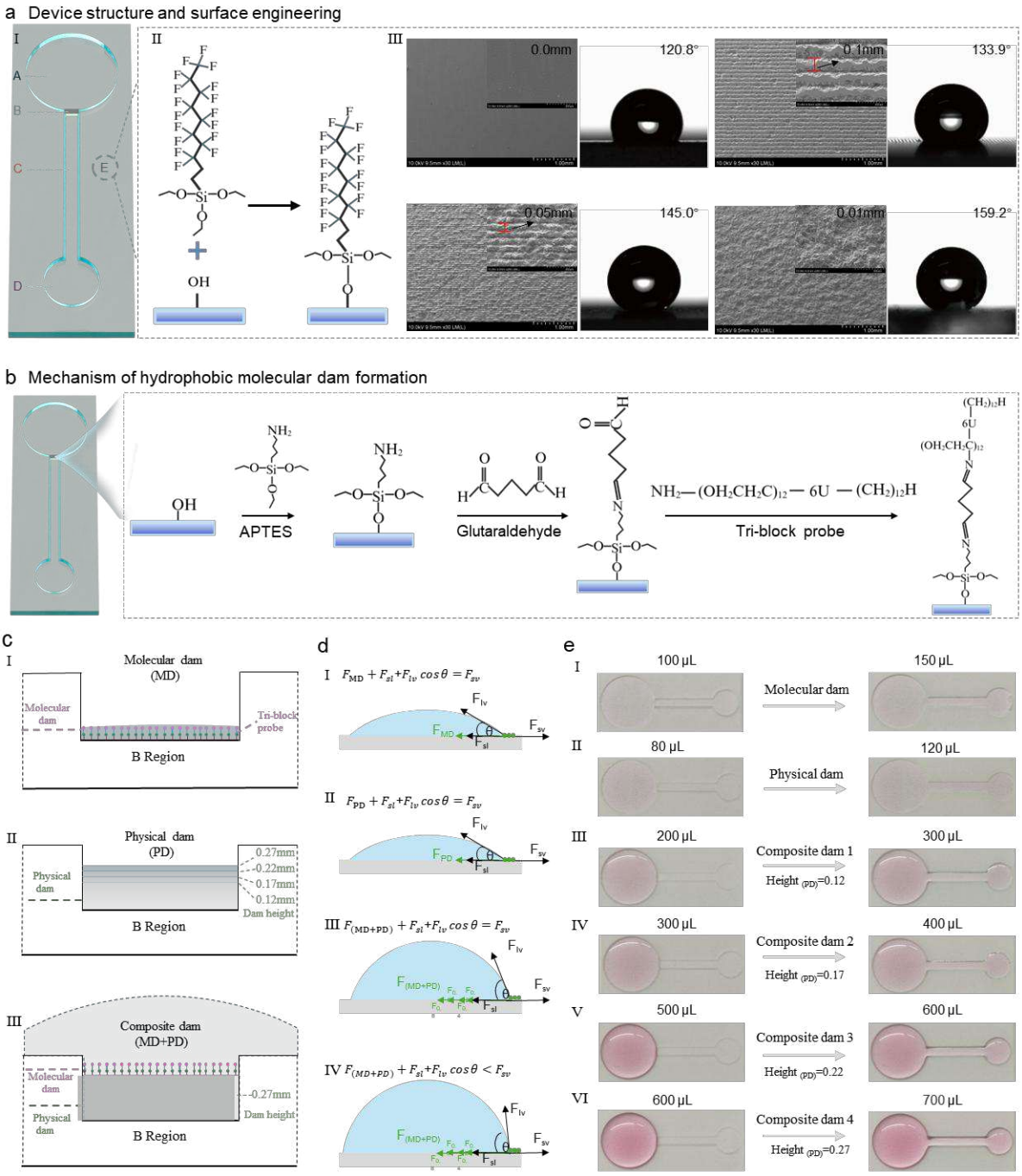


Figure 2 | Design and optimization of the chip structure. (a) Chip structure and surface engineering. Schematic of the chip layout (**aI**), comprising five functional zones: sample reservoir (A), dam (B), channel (C), collection zone (D) and exterior surface (E). Hydrophobic treatment for the E region using FAS-17(**aII**). Hydrophobic degree of the E region with different surface structure under identical FAS-17 modification (**aIII**). **(b)** Mechanism of immobilizing tri-block probe to form

hydrophobic dam. Schematic illustrating the covalent conjugation of the aminated tri-block probe onto the APTES-functionalized molecular dam (region B) via glutaraldehyde crosslinking. **(c)** Dam design. Alone molecular dam formed by tri-block probe (**cI**); Alone physical dam formed by raised chip substrate with different height (**cII**); Composite dam integrating both molecular dam and physical dam (**cIII**). (d) Force profiles of liquid in region A for distinct B-region designs: molecular dam alone (**dI**), physical dams with varying heights (**dII**), composite dam (**dIII**) and force evolution upon increasing liquid volume in the composite configuration (**dIV**). (e) Influence of B-region structures on threshold formation in region A: threshold states formed with molecular dam alone (**eI**) or physical dam alone (**eII**); Evolution of threshold states as the height of the composite dam increases from 0.12 mm to 0.27 mm (**eIII–eVI**).

Structural strategy to create a threshold-confined droplet. To maximize the chip′s sensitivity, it is essential to engineer a structural design with intrinsic signal amplification capability. We aimed to establish a critical state where a liquid droplet—much larger in volume than the underlying sample reservoir—remains stable at the drainage threshold. This configuration makes it susceptible to a "dam-break drainage" event triggered by even slight degradation of the tri-block probes. We realized this concept by designing a hydrophobic E region and a hydrophobic B region to confine the oversized droplet and prevent it from overflowing or collapsing beyond the A region (Fig. 2aI and S1). This two-step process began with laser micromachining to create a micro-nanostructured surface, followed by chemical modification with fluoroalkyl silane (FAS-17) to introduce hydrophobic groups[25, 26] (Fig. 2aII). As shown in Fig. 2aIII, the E region displayed a superhydrophobic contact angle of 159.2° under a laser matrix scanning interval of 0.01 mm (Laser power and scanning speed are provided in Table S1).

For the B region, hydrophobic modification was realized by covalently anchoring amine-modified tri-block probes onto the amine-modified B region via glutaraldehyde crosslinking (Fig. 2b). The surface amine modification of B region was performed by 3-Aminopropyltriethoxysilane (APTES)[27]. Then, we evaluated the dam′s containment efficacy against tri-block probe. As shown in Fig. S2, a tri-block probe concentration of 1 μM enabled the B region to completely prevent liquid leakage from the A region. However, this configuration limited the A region′s capacity to merely 100 μL (Fig. 2 eI). Under this condition, the liquid in A region experiences the following forces at the interface of B region (Fig. 2dI):

$$F_{MD} + F_{sl} + F_{lv}cos\theta = F_{SV} \quad (1)$$

Here, F_{MD} denotes the resistance exerted by the molecular dam; F_{sl} is the solid-liquid interfacial force; F_{lv} represent the liquid-air interfacial force; F_{sv} represent the solid-air interfacial force and θ is the contact angle between the liquid and the dam surface. When the volume in region A exceeds 100 μL, the contact angle (θ) between the liquid and the dam surface increases, leading to a decrease in F_{lv}cosθ. This shifts the force balance to:

$$F_{MD} + F_{sl} + F_{lv}cos\theta < F_{SV} \quad (2)$$

Consequently, the liquid in A region overflow into C and D regions. However, the testing liquid volume of 100 μL in A region was insufficient to form the desired hemispherical "threshold" droplet. Similarly, a standalone physical dam also fails to establish this threshold state and hard to perform sensing (Fig. 2cII, and 2eII). Specifically, when the liquid volume in region A was 80 μL, the liquid in A region was subjected to forces as depicted in Fig. 2 dII:

$$F_{PD} + F_{sl} + F_{lv}cos\theta = F_{SV} \quad (3)$$

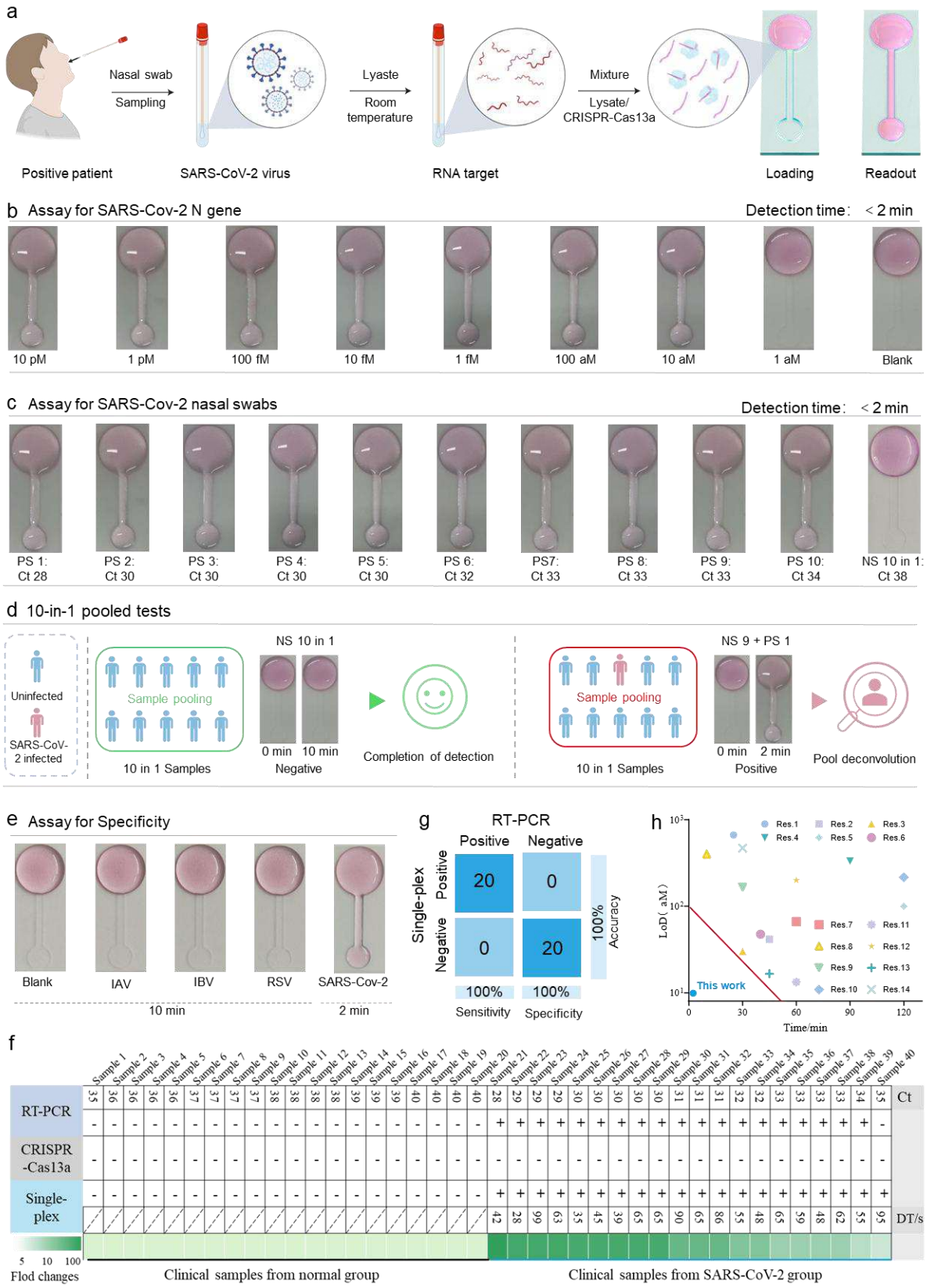


Figure 3 | Performance evaluation of the single-plex chip for SARS-CoV-2 detection. (a) Workflow schematic for SARS-CoV-2 detection. **(b)** Detection of serial dilutions of the SARS-CoV-2 N gene ranging from 1 aM to 10 pM. **(c)** Analysis of clinical nasal swab samples with Ct values between 28 and 34. **(d)** 10-in-1 pooled testing: negative pools were confined, whereas pools containing a single positive sample produced a distinct "dam-break drainage" signal within 2 min. **(e)** Specificity assessment using Influenza A virus, Influenza B virus and respiratory syncytial virus (RSV)samples; only SARS-CoV-2

triggered the "dam-break drainage" signal. **(f)** Comparative evaluation of detection performance among the single-plex chip, RT-PCR and CRISPR-Cas13a. **(g)** Confusion matrix relative to clinical RT-PCR results, indicating 100% sensitivity, specificity and accuracy. **(h)** Benchmarking of the developed chip against previously reported detection technologies.

where F_{PD} represents the resistance provided by a standalone physical dam. Under this condition, the liquid remained stably confined within region A. However, when the liquid volume exceeded 80 μL, the force balance in region A changed to:

$$F_{PD} + F_{sl} + F_{lv}cos\theta < F_{SV} \quad (4)$$

As a result, the liquid from A region spilled over into C and D regions (Fig. 2eII). To bridge this gap, we developed a composite dam (Fig. 2cIII). Unlike the alone molecular dam, this composite structure incorporates a microscale glass protrusion in the B region, upon which the tri-block probes were immobilized. To identify the optimal dam dimensions required to form a hemispherical droplet, we fixed the dam width at 90 μm and systematically varied its height from 0.12 to 0.27 mm by adjusting the laser etching power (Fig. S3). Progressively raising the height increased the sample retention volume from 150 μL to 600 μL (Fig. 2eIII-2eVI). Similarly, when the height of the physical dam within the composite dam increased to 0.27 mm and 600 μL of liquid was loaded into A region, the forces acting on the liquid at the interface between A and B regions were as shown in Fig. 2dIII:

$$F_{(MD+PD)} + F_{sl} + F_{lv}cos\theta = F_{SV} \quad (5)$$

Where $F_{(MD+PD)}$ represents the resistance provided by the composite dam. Upon further increasing the liquid volume in A region, the force balance changes to (Fig. 2dIV):

$$F_{(MD+PD)} + F_{sl} + F_{lv}cos\theta < F_{SV} \quad (6)$$

However, when the physical dam height within the composite dam reaches 0.27 mm, the chip can confine 600 μL of liquid within A region, establishing an ideal threshold state that remains poised for target-triggered breakthrough (Fig. 2eVI). Logically, for a given dam height, a narrower dam facilitates the "dam-break drainage" by requiring less probe degradation, thus improving detection sensitivity. Next, we tuned the dam width from 60-140 μm by adjusting the laser etching pattern (Fig. S4). When the width was below 90 μm, the tri-block probe-modified surface is too narrow to provide adequate hydrophobicity. In this case, the liquid failed to be confined in A region, irrespective of target presence. When the dam width ranged from 90 to 100 μm, the liquid is stably confined within A region in the absence of targets, whereas the presence of targets produced a distinct "dam-break drainage" signal. Conversely, when the dam width exceeded 100 μm, the liquid was confined within region A regardless of the presence or absence of the target. This is attributed to the interface-dependent and layer-by-layer degradation of the tri-block probes mediated by activated Cas13a on the molecular dam. The tri-block probes that were directly contact with the liquid are cleaved first, with subsequent degradation occurring progressively. At excessive dam widths, the activated Cas13a protein cannot degrade the tri-block probes across the entire dam. Under this condition, the single-plex chip fails to detect the target nucleic acid. Therefore, we determined 90 μm in width and 0.27 mm in height as the optimal configuration for the physical dam.

The single-plex chip achieved clinical-grade accuracy within minutes. As shown in Fig. 3, we evaluated the performance of the single-plex chip in detecting infectious pathogens using SARS-CoV-2 as a model. As shown in Fig. 3a, SARS-CoV-2 detection is achieved simply by adding a mixture of the target nucleic acid

and the CRISPR-Cas13a to the sample reservoir, with the presence or absence of liquid flow providing a direct visual readout. Before testing the full-length SARS-CoV-2 RNA (29,903 nt)[28], we first assessed the chip′s response to the N gene (1,260 nt)[29] to validate its feasibility. Due to the target-sequence dependence

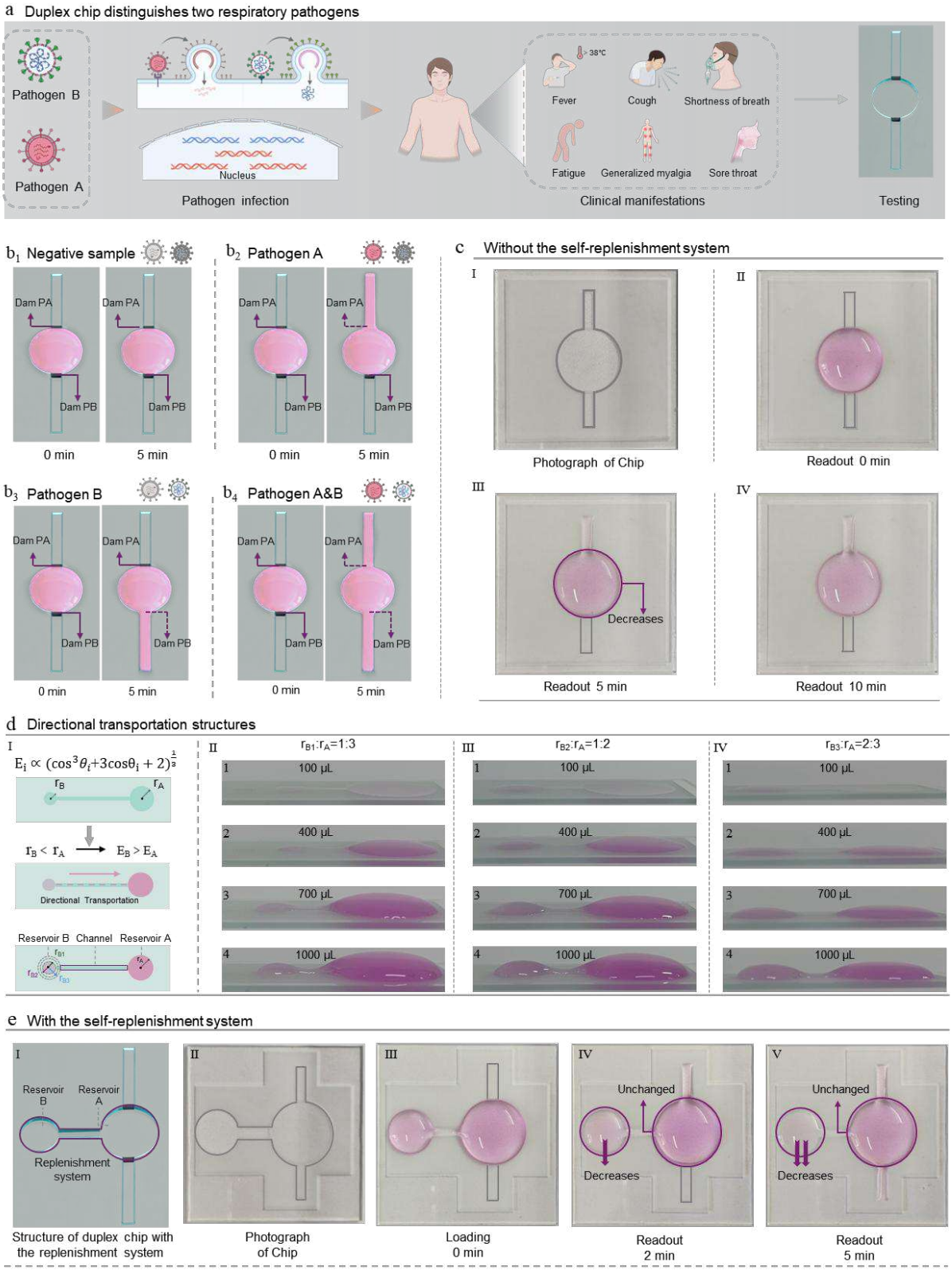


Figure 4 | Design and performance of the duplex chip in detecting two pathogens. (a) Schematic of the duplex chip designed to differentiate two respiratory pathogens (PA and PB) with similar symptoms. **(b)** Representative results showing

chip′s response to: negative sample **(b_1)**; sample containing only PA **(b_2)**; sample containing only PB **(b_3)**; sample containing both PA and PB **(b_4)**. "Dam-break drainage" signals specific to each pathogen dam (Dam PA or Dam PB) appear within 5 min. **(c)** Limitation of the chip without a self-replenishment system. Image of the duplex chip **(cI)**. Sequential images demonstrate that with a finite sample volume, only the first target is detected, as the liquid is consumed and cannot initiate the second "dam-break drainage" signal **(cII-cIV)**. **(d)** Directional transportation structure. Schematic of the directional transportation mechanism **(dI)**. Demonstration of the system's efficacy across different r_B:r_A ratios, showing sustained operation with liquid volumes from 100 to 1000 μL **(dII-dVII)**. **(e)** Enhanced performance with integrated self-replenishment. Design of the optimized duplex chip with the self-replenishment system **(eI)**. Photograph of the fabricated chip **(eII)**. Sequential detection of two targets from a mixed sample: the first target is detected at 2 min, followed by the second at 5 min, enabled by continuous liquid supply from the self-replenishment reservoir (**eIII-eV**).

of CRISPR-Cas13a′s activity, we selected the optimized N gene region spanning nucleotides from 38 to 65 as the recognition site[30-32]. As shown in Fig. 3b, Fig. S5 and Movie S1, the chip enabled rapid (within 2 min), highly sensitive detection of the SARS-CoV-2 N gene over a wide concentration range (1 aM-10 pM), with a limit of detection (LOD) of 10 aM. Compared with the conventional RT-PCR assay, the developed chip achieves both a lower detection limit and a faster readout, whereas RT-PCR fails to detect the N gene at 10 aM, yielding Ct values that overlap with the blank (Fig. S6).

Given the outstanding performance in N gene detection, we next evaluated the chip′s response to full-length SARS-CoV-2 RNA of nasal swabs to validate its performance in complex matrices (Fig. 3c). During clinical testing, RNases in sample matrices will work as the activated Cas13a protein to degrade tri-block probes, causing false-positive signals. To overcome this, we optimized the sample pretreatment protocol. As shown in Fig. S7a, complete RNase inhibition for throat swabs required both heating to lysate and the addition of RNase inhibitor (RRI). While for nasal swabs, adding RRI to lysate was sufficient to inactivate RNases without the need for heating (Fig. S8a). Notably, room-temperature lysis of nasal swabs provided higher RNA extraction efficiency than heating lysis (Fig. S9). We further confirm that the activity of CRISPR-Cas13a will not be compromised by the addition of RRI alone or in combination with the lysate (Fig. S7b, S8b and S10). Based above, we select nasal swabs as sampling resource for easy operation and instrument-free detection. In assay, ten RT-PCR positive nasal swabs (Ct=28-34) and ten RT-PCR pooled negative nasal swabs (Ct=38) were tested (Fig. S11). As a result, all positive samples generated a "dam-break drainage" signal within 2 min (Fig. S12a and Movie S2), while all negative samples were confined in the sample reservoir even after 10 min. We further evaluated chips′ performance in pooled testing scenarios, which are advantageous for large-scale screening and cost reduction. Fig. 3d shows that pooled samples containing one positive sample and nine negative samples triggered the "dam-break drainage" signal within 2 min, whereas fully negative pooled samples remained blocked after 10 min. To assess specificity, the chip was tested against three common respiratory viruses-H1N1[33, 34], IBV[35, 36] and respiratory syncytial virus[37]. As shown in Fig. 3e, the "dam-break drainage" response was exclusively triggered by SARS-CoV-2, while all other viruses showed blank-like responses over 10 min. Finally, we evaluated its clinical accuracy using 40 nasal swab samples (RT-PCR-negative samples, n=21 and RT-PCR-positive samples, n=19, Fig. 3f). Impressively, the single-plex chip sensitively identified positive samples with Ct values up to 35, while the pure CRISPR-Cas13a system failed to distinguish any positive samples from negative samples, even Ct values down to 28. Confusion matrix analysis indicated that the chip achieved 100% sensitivity, specificity

and accuracy (Fig. 3g), outperforming RT-PCR (sensitivity 95%, specificity 100%, accuracy 97.5%; Fig. S12b). Compared to other detection platforms, including diagnostics with coronavirus enzymatic reporting (DISCoVER)[38], colorimetric detection[39] and CRISPR-Cas13a cascade-based viral RNA (Cas13C) assay[40], our single-plex chip demonstrates better detection limit and speed (Fig. 3h and Table S2).

An energy-driven self-replenishment strategy for reliable duplex detection. As shown in Fig. 4a, respiratory infections caused by different pathogens often exhibit overlapping clinical manifestations. For example, Influenza A virus infection typically causes fever, headache and cough, symptoms that closely resemble those of Influenza B virus and other respiratory viruses[41]. Consequently, relying solely on clinical symptoms makes it difficult to accurately determine the underlying pathogen, leading to potential misdiagnosis or delayed treatment. To address this issue, we further developed a duplex chip capable of simultaneously identifying two pathogens. As shown in Fig. 4b, the detection mode of duplex chip are

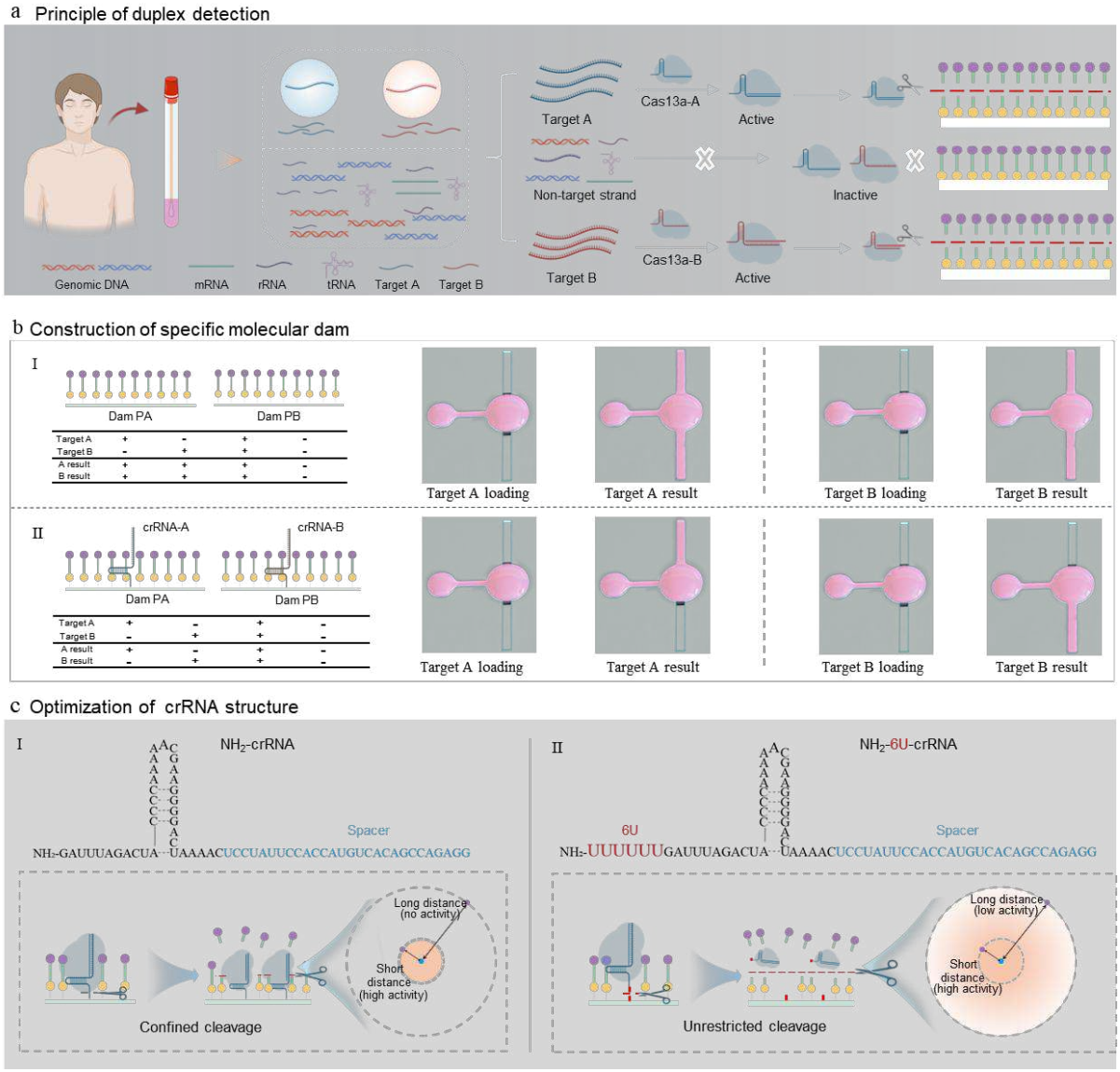


Figure 5 | Engineering specific molecular dams and optimizing crRNA architecture for duplex detection. (a) Working principle: two target RNAs orthogonally activate their respective CRISPR-Cas13a systems, leading to the specific cleavage of their corresponding tri-block probes on the molecular dams. **(b)** Formation of specific molecular dams: A non-specific dam, constructed from tri-block probes alone, is susceptible to be break by any activated Cas13a, leading to potential false-positive signals **(bI)**. A specific molecular dam, incorporating both tri-block probes and matched crRNA, ensures that drainage occurs

only upon recognition of the intended target, thereby conferring specificity **(bII)**. **(c)** Overcoming spatial confinement of Cas13a. Direct immobilization of the crRNA anchors the activated Cas13a protein, limiting its collateral cleavage to adjacent tri-block probes **(cI)**. Engineering a 6U spacer that acts as a flexible tether between the amino group and crRNA allows partial mobility after Cas13a activation, thereby expanding the effective cleavage radius and enhancing tri-block probe degradation **(cII)**.

operated as follows: when the detection solution is added into the sample reservoir, the presence of pathogen A (PA) nucleic acid triggers a "dam-break drainage" signal at Dam PA (similarly for pathogen B), whereas the coexistence of two viral targets generate signals in both Dam PA and Dam PB. However, a critical challenge arises from the chip′s structural design (Fig. 4c): once one target nucleic acid induces the "dam-break drainage" event, the liquid volume in the sample reservoir decreases significantly. This diminishes the threshold state required for the subsequent "dam-break drainage" redout, thereby reducing the detection sensitivity of the other target and even leading to "false-negative results". To address this issue, we engineered the duplex chip with a self-replenishment system based on a directional transportation structure[42] (Fig. 4dI,). The directional transportation structure comprised reservoir A, channel and reservoir B. When the dimension of reservoir B is smaller than that of reservoir A, the liquid in reservoir B presents a higher surface energy (E_B) than that in reservoir A (E_A). The surface energy difference spontaneously drives liquid directional transport from reservoir B to reservoir A[43]. Under a fixed channel, we systematically investigated the effect of dimension ratio between reservoir B and reservoir A (r_B:r_A) on directional transport efficiency. As shown in Fig. 4dII and Movie S3, when r_B:r_A=1:3, liquid added to reservoir B will smoothly be transferred to reservoir A. Reservoir A collects most of the liquid and only a minimal amount retained in reservoir B, a trend consistent across volumes from 100 μL to 1000 μL. Similarly, when r_B:r_A=1:2, the liquid also will be automatically transferred from reservoir B to reservoir A except for a small amount of liquid began to accumulate in reservoir B, as the loading volume growing from 100 to 1000μL (Fig. 4dIII). When the ratio was set to 2:3, the liquid initially accumulated in reservoir B and then gradually flowed into reservoir A. As the loading volume increased, substantial liquid accumulation occurred in both reservoirs, while the liquid increment in reservoir A being markedly greater than that in reservoir B (Fig. 4dIV). The directional transportation structure is promising to resolve the challenge in duplex detection, where the liquid volume reduction induced by the first target disrupts the drainage threshold and consequently impairs the sensitivity of the subsequent target detection. Thus, we incorporated this directional transportation structure into the duplex chip, equipping it with a self-replenishment capability. (Fig. 4eI and 4eII). However, this design involves a trade-off between the efficiency and capacity of the self-replenishment process. As shown in Fig. S13, at r_B:r_A ratios of 1:3 or 1:2, the self-replenishment system responded promptly to the first target, while the replenished liquid volume was inadequate to maintain the drainage threshold, as reservoir B initially retained only a limited amount of liquid. In contrast, when the ratio of r_B:r_A was increased to 2:3, the system achieved a more balanced performance. It not only ensured efficient directional liquid transfer after the first detection event but also supplied sufficient replenishment to preserve the drainage threshold, thereby supporting reliable dual-target detection. As shown in Fig. 4eIII and 4eIV, after the first target triggered the "dam-break drainage" event, reservoir A maintained a constant liquid volume while reservoir B performed a decreased fluid volume. Then, the second target was reliably detected within 5 min, during which the liquid in A reservoir maintains threshold state continuously (Fig. 4eV).

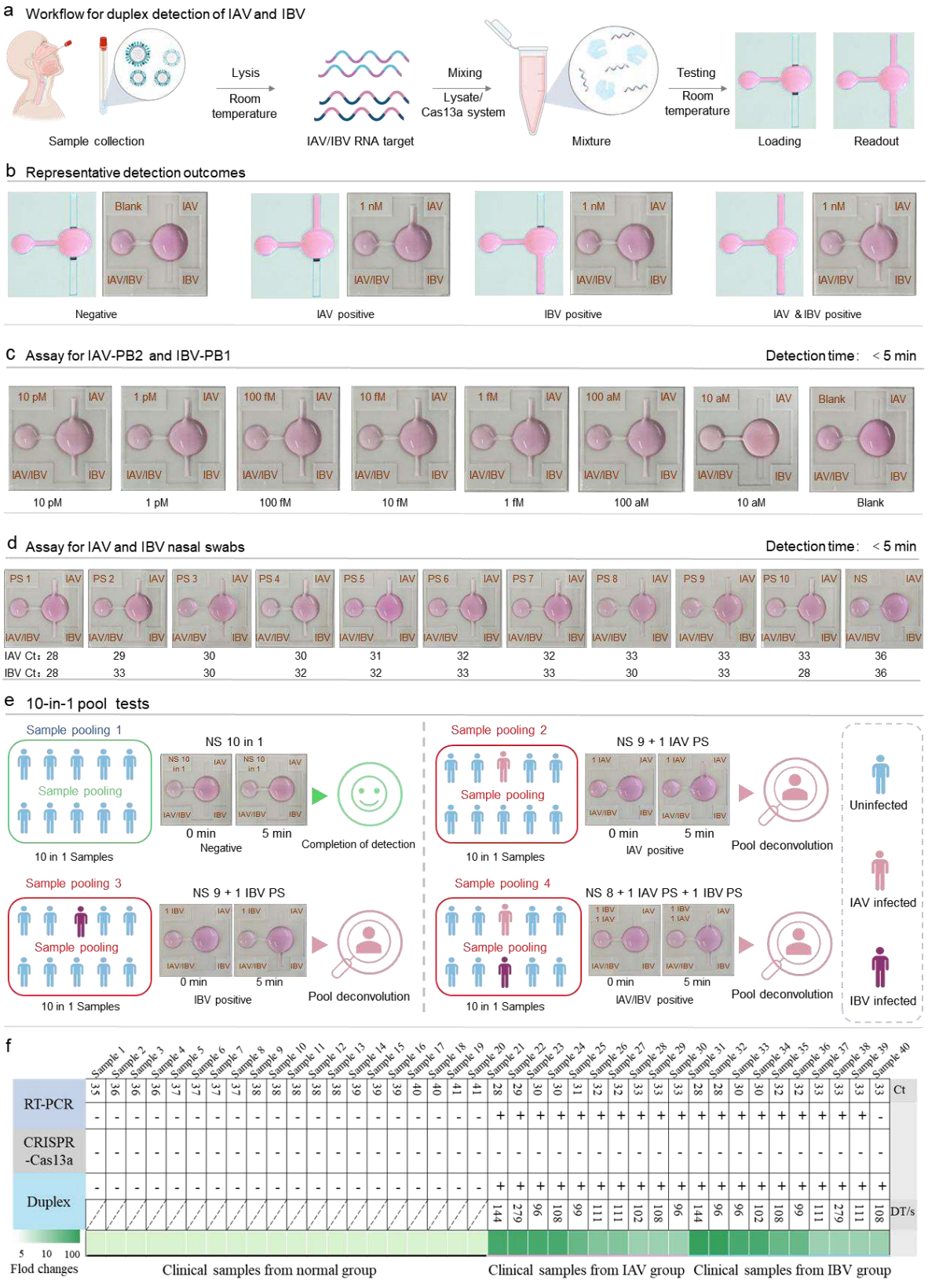


Figure 6 | Duplex chip evaluation for Influenza A and B virus detection. (a) Schematic illustration of the workflow for duplex detection of IAV and IBV on the duplex chip. **(b)** Representative detection outcomes for negative, IAV-positive, IBV-positive and dual-positive samples. The "dam-break drainage" signal appears exclusively at the corresponding channel within 5 min, indicating high target specificity. **(c)** Analytical sensitivity assessment using serial dilutions (10 aM–10 pM) of synthetic IAV-PB2 and IBV-PB1 RNA targets at equal concentrations. **(d)** Clinical validation with nasal swab samples: pooled analysis

of ten IAV-positive (Ct=28-33) and ten IBV-positive (Ct=28-33) clinical specimens showed accurate target identification without cross-reactivity. **(e)** 10-in-1 pooled testing: the negative pool produced no drainage signal, whereas pools containing a single IAV-positive or IBV-positive sample generated distinct signals on their respective sides within 5 min. Dual-positive pools triggered synchronous drainage signals on both channels. **(f)** Comparative analysis of detection performance across the duplex chip, RT-PCR and CRISPR-Cas13a assays, confirming consistent diagnostic accuracy and reliability.

A dam-anchored and self-releasing crRNA design to restore selective and efficient Cas13a activation. In the single-plex assay, SARS-CoV-2 detection is simply achieved by adding a mixture of the target nucleic acid and the CRISPR-Cas13a solution to the sample reservoir, with the presence or absence of liquid flow providing a direct visual readout. However, this strategy is not applicable to the duplex chip, where two distinct targets both can trigger the tri-block probe degradation (Fig. 5a). The CRISPR-Cas13a activated by either target would cleave the probes in both dams, resulting in a complete loss of detection specificity (Fig.5bI). To address this issue, we functionalized the 5' end of the crRNA with an amino group for covalent immobilization on different dams (Fig. 5bII). In this configuration, each molecular dam contains both the tri-block probes and crRNAs that specifically recognize the fixed pathogen nucleic acid. During detection, each pathogen′s nucleic acid specifically activates only its cognate CRISPR-Cas13a complex within the fixed channel, which in turn cleaves the nearby tri-block probes. This strategy effectively eliminates cross-reactivity and prevents false-positive signals. The amino-modified crRNAs do not affect the RNase activity of the Cas13a protein (Fig. S14). Although this strategy successfully ensures specificity, it introduces a new limitation: once the CRISPR-Cas13a complex is immobilized on the molecular dam, the activated Cas13a proteins are spatially confined and can only degrade the nearby tri-block probes (Fig. 5cI). This constraint significantly weakens the overall degradation efficiency and hampers the wettability transition of the dam surface, thereby limiting the detection sensitivity. To overcome this, we further optimized the crRNA design by inserting a Cas13a-responsive linker (6U) between the amino group and the crRNA sequence (Fig. 5cII). Upon target recognition, the activated Cas13a cleaves this linker, transiently releasing the local Cas13a-crRNA complex into a quasi-free state. This allows the activated Cas13a to degrade a broader range of the tri-block probes surrounding the molecular dam, resulting in a more efficient wettability transition and markedly enhanced detection sensitivity.

The duplex chip offered reliable pathogens identification in synthetic fragments, clinical samples and pooled scenarios. As shown in Fig. 6, we employed Influenza A virus (IAV)[44] and Influenza B virus (IBV)[45, 46]—two common respiratory pathogens—as models to evaluate the duplex chip′s capability for simultaneous dual-target detection. As shown in Fig. 6a, for duplex detection, the result can be interpreted simply loading the mixture of lysate/Cas13a protein and observing whether a “dam-break drainage” signal appeared in fixed channel. Before testing full-length IAV and IBV RNA, we first examined the chip′s performance toward the IAV-PB2 (314-342 nt)[47] and IBV-PB1 (1296-1324 nt)[46] gene fragments. The corresponding crRNAs were immobilized on the molecular dams of two separate channels. As shown in Fig. 6b and Movie S4-S6, in the absence of targets, the liquid is confined within the sample reservoir with no observable flow; in contrast, the presence of the IAV-PB2 gene alone triggers a “dam-break drainage” signal specifically in the IAV channel; Similarly, the presence of the IBV-PB1 gene alone triggers a “dam-break drainage” signal specifically in the IBV channel; when both targets coexisted, the chip sequentially detected each target. As shown in Fig. 6c, S15 and Movie S7, when IAV-PB2 and IBV-PB1 RNA targets were mixed at equal

concentrations within the range of 10 aM to 10 pM, the duplex chip successfully distinguished the two targets independently within 5 min, maintaining a detection limit of 100 aM. The detection performance of the duplex chip rivals that of conventional RT-PCR assays (Fig. S16 and Fig. S17).

To assess the potential for real-world use, the chip performance was further examined by testing ten groups of randomly mixed IAV RT-PCR-positive (Ct=28-33, Fig. S18) and IBV RT-PCR-positive samples (Ct=28-33, Fig. S19) were analyzed. Both detection channels produced distinct "dam-break drainage" signals within 5 min, whereas negative samples were confined in the sample reservoir without any "dam-break drainage" signal even after 10 min (Fig. 6d, Fig. S20a and Movie S8). These results confirm that the duplex chip can reliably identify target nucleic acids in clinically derived complex matrices. Given the established advantages of pooled testing for large-scale screening, we systematically evaluated the performance of our duplex chip under these conditions. Four groups were prepared: (i) ten negative samples, (ii) one IAV-positive sample mixed with nine negative samples, (iii) one IBV-positive sample mixed with nine negative samples and (iv) one IAV-positive sample and one IBV-positive sample mixed with eight negative samples. As shown in Fig. 6e, each positive pool triggered a "dam-break drainage" signal exclusively in the fixed channel, while the dual-positive pool generated signals in both channels. Conversely, the liquid in the negative pool remained entirely restricted to the sample reservoir. We evaluated the clinical performance of the duplex chip by IAV-positive samples (n=10), IBV-positive samples (n=10) and negative samples (n=20). As summarized in Fig. 6f and Fig. S18a, both RT-PCR and our duplex chip assay correctly identified all IAV-positive, IBV-positive and negative samples, while the duplex chip delivering results in a significantly shorter time. In contrast, the CRISPR-Cas13a system alone failed to discriminate between positive and negative samples. Confusion matrix analysis confirmed that, against RT-PCR as the reference method, our dual-detection chip achieved 100% sensitivity, specificity and accuracy for both targets (Fig. S20b). A comparative analysis with previously reported methods for IAV and IBV detection[48, 49] (Fig. S20c and Table S3) demonstrated that the duplex chip achieves superior sensitivity and faster response, highlighting its potential for early screening and precision diagnosis.

Discussion

In this study, we developed single-plex and duplex chip based on a target-activated CRISPR-Cas13a system that mediates a wettability switching at the solid-liquid interface, combined with a "dam-break drainage" readout. Both platforms exhibit three key advantages: First, the chips are fabricated using simple and low-cost processes, with total material expenses kept below $0.2 per test. This affordability makes them particularly suitable for large-scale screening in resource-limited settings and low-to-middle-income countries. Second, neither chip requires external temperature control or complex instrumentation. They achieve attomolar-level sensitivity within minutes at room temperature, underscoring their utility for early pathogen detection and potential use in rapid at-home self-testing. Third, we demonstrated the high performance of both platforms in pooled testing, where they outperformed commercially available amplification kits in both sensitivity and speed. These results indicate the potential of our chips to serve as a new, versatile nucleic acid testing technology. One shortcoming of this method is that the current versions are limited to qualitative detection and do not support quantitative analysis. Future work will focus on developing quantification strategies and expanding multiplexing capability. It is also worth noting that while

the current chips rely on CRISPR-Cas13a for nucleic acid recognition, the underlying design principle can be adapted to other classes of biomarkers. With ongoing advances in molecular biology and materials science, a wide range of targets—including proteins, bacteria, exosomes and small molecules—can induce detectable physical or chemical responses, such as pH changes, enzymatic activity modulation, or interfacial property shifts. By re-engineering the responsive module in the molecular probe, the platform could be extended to detect diverse biomarkers, positioning it as a generalizable bioanalytical tool for multi-analyte testing.

Materials and Methods

Materials. Glass slides were purchased from Yufan Laboratory Equipment Co., Ltd. (Yancheng, Jiangsu, China). 1H,1H,2H,2H-Perfluorodecyltrimethoxysilane (FAS-17), 3-Aminopropyltriethoxysilane (APTES), glutaraldehyde (50%) and phosphate-buffered saline (10×PBS) were purchased from Aladdin Reagent Co., Ltd. (Shanghai, China). Toluene and ethanol were obtained from Sinopharm Chemical Reagent Co., Ltd. TaqProbe 2×qPCR-Multiplex Premix and RNase Inhibitor (RRI) were obtained from Sangon Biotech Co., Ltd. (Shanghai, China). The SARS-CoV-2 N gene plasmid (pUC57-2019-nCoV-N), the Influenza A virus (IAV-PB2) target, Influenza B virus (IBV-PB1) target and respiratory syncytial virus (RSV) target were obtained from GenScript (Nanjing, China). The DNA amplification kit, all TaqMan probes, all forward primers, all reverse primers, tri-block probes, all crRNAs, InviTrans T7 In Vitro Transcription Kit (AG51201) and SteadyPure RNA Extraction Kit (AG21017) were purchased from Accurate biotechnology (Hunan) Co., Ltd. (changsha, China). NEBuffer 4 was obtained from New England Biolabs International Trading Co., Ltd. (Shanghai, China). LwaCas13a protein was purchased from Huicheng Biotechnology Co., Ltd. (Shanghai, China). The lysis buffer was purchased from Shandong Huifan Medical Instrument Co., Ltd. (China). A laser pattern system was obtained from Wuhan Harmonious Horizon Laser Equipment Co., Ltd. (Wuhan, China). PCR amplification, real-time quantitative PCR analysis and nucleic acid quantification were performed using an Applied Biosystems 2720 Thermal Cycler, the StepOne Real-Time PCR System and a Thermo Fisher NanoDrop One spectrophotometer, respectively. The sequences of all nucleic acids used in this work are provided in Table S4-S8.

Protocol for the single-plex chip

Step 1. Structure pattern for chip surface: The glass slide (76.2 mm×25.4 mm) surface was patterned with microstructure ready for chemical modification by the laser pattern system. The pattern measures 22 mm in width and 43 mm in length, which works as the chip substrate (Fig. S21a step I, S21bI-S 21bII and Table S9). The detailed laser settings are provided in Table S1.

Step 2. FAS-17 treatment (Fig. S21a step II): The laser-treated glass slide was immersed in a 0.1% (v/v) FAS-17/toluene solution and reacted at room temperature for 60 min. Then the modified glass slide was washed with deionized water and ethanol. Finally, the obtained glass slide was dried at 60℃ for 5 min.

Step 3. Functional zones pattern: Four functional zones were patterned on the chip substrate using the laser pattern system. The detailed dimensions of four patterned zones are shown in Fig. S21a step III, S21bIII-S 21bVI and Table S9.

Step 4. APTES treatment: As shown in Fig. S21a step IV, to achieve amination of the chip surface, the glass slide was immersed in a 60% (v/v) APTES/ethanol solution and react at room temperature for 60 min. Then

the glass slide was washed with ethanol and dried at 60℃ for 5 min.

Step 5. Glutaraldehyde treatment: In order to immobilize the amino modified tri-block probe on region B to form dam, the chip surface was further modified with aldehyde group by reacting with glutaraldehyde solution (pH 7.5) at room temperature for 60 min. Then, the glass slide was sequentially washed with deionized water and ethanol. Finally, the glass slide was dried at 60℃ for 5 min (Fig. S21a step V).

Step 6. Probe immobilization: As shown in Fig. S21a step VI, the 5' end aminated tri-block probe was immobilized on the chip surface via an amine-aldehyde condensation reaction. Briefly, 600 μL of a 1 μM probe solution in ethanol was introduced into the chip and allowed to react at room temperature for 60 min. Subsequently, the chip was rinsed with ethanol and dried at room temperature for 30 min.

Step 7. Region B construction: The immobilized tri-block probe was removed from chip surface except for those in region B by using the laser pattern system to form the molecular dam (Fig. S21a step VII).

Procedure for the single-plex chip detection. 10 μL of target solution was mixed with 590 μL of CRISPR-Cas13a reagent containing 60 μL of 10×NEBuffer 4, 5 μL of LwaCas13a protein (final concentration, 80 nM), 2 μL of crRNA (final concentration, 40 nM), 33 μL of phenol red solution (200 mg/L) and 490 μL of RNase-free water. The 600 μL mixture was then loaded into the single-plex chip for detection.

SARS-CoV-2 N gene preparation. The SARS-CoV-2 N gene was prepared using the following procedure: Step 1 (Amplification): An amplification mixture (50 μL total volume) was prepared, consisting of 100 ng plasmid DNA (SARS-CoV-2 N gene plasmid, pUC57-2019-nCoV-N), 2.5 μL forward primer(final concentration, 500 nM), 2.5 μL reverse primer (final concentration, 500 nM) and 25 μL TaqProbe 2×qPCR-Multiplex Master Mix (BBI, B630005). The reaction was then subjected to thermal cycling following the TaqProbe 2×qPCR-Multiplex Master Mix′s instructions. Step 2 (Transcription): A 50 μL transcription mixture containing 8 μL amplified product, 5μL 10×In vitro transcription buffer, 20 μL NTP Mix, 5 μL T7 RNA Polymerase Mix and 12 μL RNase free water was incubated at 37°C for 5 h. Subsequently, 5 U DNase I was added to digest the DNA template. Step 3 (Purification and quantification): The transcribed RNA was purified with the SteadyPure RNA Extraction Kit (AG21017) and quantified using a NanoDrop spectrophotometer. The sequences of the used primers are shown in Table S4.

RT-PCR kit for RNA detection. To benchmark the chips performance against the gold standard RT-PCR, RNA amplification was conducted using a one-step RT-qPCR probe kit (BBI, B639278). We employed the U.S. Centers for Disease Control and Prevention (CDC)-recommended N2 RT-PCR target site for SARS-CoV-2 N gene detection, amplifying the corresponding fragment with gene-specific TaqMan probe, forward primer and reverse primer on the StepOne Real-Time PCR System. Detection of Influenza A and B genes (IAV-PB2 and IBV-PB1) followed the same procedure, with the corresponding TaqMan probe and primers sets substituted. For clinical samples, the lysates of nasal swabs were directly used as templates. The sequences of all oligonucleotides are provided in Table S5.

RNase activity test of Cas13a with modified crRNAs. A 10 μL reaction mixture containing 1 μL LwaCas13a (final concentration, 40 nM), 1 μL modified crRNA (final concentration, 20 nM), 1 μL ssRNA reporter (6U FAM–BHQ final concentration, 1 μM), 1 μL SARS-CoV-2 N gene (final concentration, 1 nM), 1 μL 10×NEBuffer 4 and 5 μL RNase-free water. Three control groups were included in this assay: Cas13a complexed with wild-type crRNA, amino-modified crRNA, or amino-6U-modified crRNA. Reactions were

incubated at 37°C and fluorescence signals were recorded every minute for 50 min using a StepOne Real-Time PCR System. Negative control was performed by replacing the target with RNase-free water.

Protocol for the duplex chip

Step 1. Structure pattern for chip surface: The surface of the 50 mm×50 mm glass slide was patterned with microstructures using the laser pattern system for subsequent chemical modification. Details are provided in Fig. S22a step I, S22bI-S22bII and Table S10.

Step 2. Functional zones pattern: The glass slide surface was patterned to form the functional zones using a laser pattern system. The detailed process and parameters are listed in Fig. S22a step II, S22bIII-S22bV and Table S10.

Step 3. FAS-17 treatment: The detailed treatment process follows step 4 of the "Protocol for the single-plex chip" (Fig. S22a step III).

Step 4. Hydrophobic isolation zone formation: To construct specific molecular dams in the duplex chip, a hydrophobic isolation zone was introduced in reservoir A, effectively partitioning the chip into two structurally independent segments (A and B) for separate crRNAs immobilization. The process and parameters of constructing the hydrophobic isolation zone are provided in Fig. S22a step IV, Fig. S22bVI and Table S10.

Step 5. APTES treatment: To functionalize the chip surface with amino groups, the glass slide was immersed in a 50% (v/v) APTES/ethanol solution and incubated at room temperature for 60 min. The slide was then rinsed with ethanol and dried at 60°C for 5 min (Fig. S22a step V).

Step 6. Glutaraldehyde treatment: To immobilize the amino-modified tri-block probe and crRNAs on the chip surface for constructing specific dams′ structure, 200 μL of glutaraldehyde solution (pH 7.5) was added to each of the two independent segments on the chip surface. Then, the chip was incubated at room temperature for 60 min to achieve aldehyde modification. After the reaction, the slide was sequentially rinsed with deionized water and ethanol. Finally, the slide was dried at 60°C for 5 min (Fig. S22a step VI).

Step 7. Probe immobilization: Since the solvent of the tri-block probe is ethanol, the hydrophobic isolation zone prepared with FAS-17 in step 4 will not introduce phase separation with solution loading. Therefore, adding the tri-block probe solution to reservoir A will effectively enable uniform immobilization across all the chip functional zones. The detailed immobilization procedure follows step 6 of "protocol for the single-plex chip" (Fig. S22a step VII).

Step 8. Position-specific immobilization of crRNA: To construct distinct molecular dams, a hydrophobic isolation zone was introduced into reservoir A during step 4, enabling crRNA1 (targeting IAV) and crRNA2 (targeting IBV) to be individually loaded into segments A and B, respectively. This strategy ensured the formation of crRNA-specific regions (segment A and segment B) without cross-interference. In detail, 200 μL of a 40 nM crRNA solution (prepared in 1×PBS) was added to each designated segment and incubated at room temperature for 60 min. Then the surface was rinsed with ethanol and air-dried at room temperature for 30 min. The overall workflow is illustrated in Fig. S22a step VIII.

Step 9. B region (Dam) constructions: As shown in Fig. S22a step IX, except for tri-block probes and crRNAs retained on dams 1 and 2, all other immobilized tri-block probes and crRNAs on the chip surface were removed using the laser pattern system to construct the specific molecular dam. In addition, the hydrophobic

isolation zone within reservoir A was ablated by the same laser pattern process, converting reservoir A into a single unified chamber for subsequent dual-target sample loading.

Step 10. Self-replenishment system construction: The glass slide surface was engineered using the laser pattern system to construct the directional transportation structure within the duplex chip. As shown in Fig. S22a step X, reservoir B was fabricated to the left of reservoir A and connected to reservoir A by a channel. Reservoir B had a radius that was two-thirds of reservoir A′s, while the channel measured 2 mm in width and 9 mm in length. The parameters are as shown in Fig. S22bVII and Table S10.

Procedure for the duplex chip detection. 10 μL of target solution was added to 990 μL of Cas13a reaction mixture consisting of 100 μL of 10×NEBuffer 4, 8 μL of LwaCas13a protein (final concentration, 80 nM), 55 μL of phenol red solution (200 mg/L) and 827 μL of RNase-free water. The resulting 1 mL mixture was loaded into the duplex chip for detection.

References

1. Yan D, Li Z, Lee MMS, Zhong Tang B, Wang D. NIR-II AIEgens for Infectious Diseases Phototheranostics. *Angew. Chem. Int. Ed.* **63**, e202414259 (2024).
2. Wells TJ, Esposito T, Henderson IR, Labzin LI. Mechanisms of antibody-dependent enhancement of infectious disease. *Nat. Rev. Immunol.* **25**, 6-21 (2025).
3. Finney J*, et al.* Protective human antibodies against a conserved epitope in pre- and postfusion influenza hemagglutinin. *PNAS* **121**, e2316964120 (2024).
4. Yang Y, Li F, Du L. Therapeutic nanobodies against SARS-CoV-2 and other pathogenic human coronaviruses. *J. Nanobiotechnol.* **22**, 304 (2024).
5. Azhar EI, Hui DSC, Memish ZA, Drosten C, Zumla A. The Middle East Respiratory Syndrome (MERS). *Infect. Dis. Clin. North Am.* **33**, 891-905 (2019).
6. Keita M, Boland ST, Okeibunor J, Chamla D, Gueye AS, Moeti M. 10 years after the 2014–16 Ebola epidemic in west Africa: advances and challenges in African epidemic preparedness. *Lancet* **403**, 2573-2575 (2024).
7. Morawska L, Li Y, Salthammer T. Lessons from the COVID-19 pandemic for ventilation and indoor air quality. *Science* **385**, 396-401 (2024).
8. Wang T-Y, Sun Y, Tang Y-D. Re-emergence of chikungunya virus in China by 2025: What we know and what to do? *PLoS Pathog.* **21**, e1013556 (2025).
9. Chen Z*, et al.* Disruption of seasonal influenza circulation and evolution during the 2009 H1N1 and COVID-19 pandemics in Southeastern Asia. *Nat. Commun.* **16**, 475 (2025).
10. Kevadiya BD*, et al.* Diagnostics for SARS-CoV-2 infections. *Nat. Mater.* **20**, 593-605 (2021).
11. Wang D*, et al.* Rapid lateral flow immunoassay for the fluorescence detection of SARS-CoV-2 RNA. *Nat. Biomed. Eng.* **4**, 1150-1158 (2020).
12. Tsang NNY, So HC, Ng KY, Cowling BJ, Leung GM, Ip DKM. Diagnostic performance of different sampling approaches for SARS-CoV-2 RT-PCR testing: a systematic review and meta-analysis. *Lancet Infect. Dis.* **21**, 1233-1245 (2021).
13. Gootenberg JS, Abudayyeh OO, Kellner MJ, Joung J, Collins JJ, Zhang F. Multiplexed and portable nucleic acid detection platform with Cas13, Cas12a, and Csm6. *Science* **360**, 439-444 (2018).
14. Chen JS*, et al.* CRISPR-Cas12a target binding unleashes indiscriminate single-stranded DNase activity. *Science* **360**, 436-439 (2018).
15. Liu P*, et al.* Creating a Modular Activatable CRISPR–Cas12a System by Engineering crRNA Scaffold with a Steric Hindrance Effector. *J. Am. Chem. Soc.* **147**, 31349-31364 (2025).
16. Umapathi R*, et al.* Versatility of MXene based materials for the electrochemical detection of phenolic contaminants. *Coord. Chem. Rev.* **525**, 216305 (2025).
17. Li M*, et al.* Dual-Atom Catalyst Au@S-rGO for Rapid and Highly Sensitive Electrochemical Detection of Fentanyl in Serum. *Adv. Sci.* **12**, 2500430 (2025).
18. Nah SH, Kim JB, Chui HNT, Suh Y, Yang S. Enhanced Colorimetric Detection of Volatile Organic Compounds Using a Dye-Incorporated Photonic Crystal-Based Sensor Array. *Adv. Mater.* **36**, 2409297 (2024).
19. Basso CR, Filho MVB, Gavioli VD, Parra JPRLL, Castro GR, Pedrosa VA. Recent Advances in Nanomaterials for Enhanced Colorimetric Detection of Viruses and Bacteria. *Chemosensors* **13**, 112 (2025).

20. Wang Y, *et al.* Ultrasensitive single-step CRISPR detection of monkeypox virus in minutes with a vest-pocket diagnostic device. *Nat. Commun.* **15**, 3279 (2024).
21. Fu Y, *et al.* Light-Switch Electrochemiluminescence-Driven microfluidic sensor for rapid and sensitive detection of Mpox virus. *Chem. Eng. J.* **498**, 154930 (2024).
22. Shan Y, Zhou X, Huang R, Xing D. High-Fidelity and Rapid Quantification of miRNA Combining crRNA Programmability and CRISPR/Cas13a trans-Cleavage Activity. *Anal. Chem.* **91**, 5278-5285 (2019).
23. Knott GJ, *et al.* Guide-bound structures of an RNA-targeting A-cleaving CRISPR–Cas13a enzyme. *Nat. Struct. Mol. Biol.* **24**, 825-833 (2017).
24. Gootenberg JS, *et al.* Nucleic acid detection with CRISPR-Cas13a/C2c2. *Science* **356**, 438-442 (2017).
25. Zhang Y, Liu Q, Li J, Yao H, Hou Y, Hou J. Large-scale fabrication of flexible antiglare film with superhydrophobic surface: Toward high transmittance and high haze. *Chem. Eng. J.* **511**, 161805 (2025).
26. Gou Q, *et al.* Enhancing nitrate reduction to ammonia by synergistic and interface coupling effects of binary metal sites. *Appl. Catal. B* **348**, 123810 (2024).
27. Sekar B, Murugan R, Thulasidhas D, Arumugam S. Evaluating the Influence of APTES‐Treated Glass Powder on Shear and Vibrational Characteristics of Co‐cured Composite Joints. *Polym. Compos.* **0**, 1-13 (2025).
28. Kim D, Lee J-Y, Yang J-S, Kim JW, Kim VN, Chang H. The Architecture of SARS-CoV-2 Transcriptome. *Cell* **181**, 914-921.e910 (2020).
29. Ayubov MS, *et al.* Profiling of the most reliable mutations from sequenced SARS-CoV-2 genomes scattered in Uzbekistan. *PLoS One* **17**, e0266417 (2022).
30. Yang H, Patel DJ. Structures, mechanisms and applications of RNA-centric CRISPR–Cas13. *Nat. Chem. Biol.* **20**, 673-688 (2024).
31. Sun Y, *et al.* A tube-based biosensor for DNA and RNA detection. *Sci. Adv.* **11**, eadu2271 (2025).
32. Li Y, Zhao Y, Yi Z, Han S. A CRISPR/Cas13a-based and hybridization chain reaction coupled evanescent wave biosensor for SARS-CoV-2 gene detection. *Analyst* **150**, 1367-1376 (2025).
33. Yang H-H, Huang IT, Wu R-C, Chen L-K. A highly efficient and accurate method of detecting and subtyping Influenza A pdm H1N1 and H3N2 viruses with newly emerging mutations in the matrix gene in Eastern Taiwan. *PLoS One* **18**, e0283074 (2023).
34. Loes AN, *et al.* High-throughput sequencing-based neutralization assay reveals how repeated vaccinations impact titers to recent human H1N1 influenza strains. *J. Virol.* **98**, e00689-00624 (2024).
35. Welch NL, *et al.* Multiplexed CRISPR-based microfluidic platform for clinical testing of respiratory viruses and identification of SARS-CoV-2 variants. *Nat. Med.* **28**, 1083-1094 (2022).
36. Zhang X, Wu X, Feng K, Wang Q, Xie Q. A New Dual Fluorescence Method for Rapid Detection of Infectious Bronchitis Virus at Constant Temperature. *Microorganisms* **12**, 1315 (2024).
37. Li H, *et al.* Amplification-Free Detection of SARS-CoV-2 and Respiratory Syncytial Virus Using CRISPR Cas13a and Graphene Field-Effect Transistors. *Angew. Chem. Int. Ed.* **61**, e202203826 (2022).
38. Chandrasekaran SS, *et al.* Rapid detection of SARS-CoV-2 RNA in saliva via Cas13. *Nat. Biomed. Eng.* **6**, 944-956 (2022).
39. Zhang T, *et al.* A paper-based assay for the colorimetric detection of SARS-CoV-2 variants at single-nucleotide resolution. *Nat. Biomed. Eng.* **6**, 957-967 (2022).
40. Wang Y, *et al.* CRISPR-Cas13a cascade-based viral RNA assay for detecting SARS-CoV-2 and its mutations in clinical samples. *Sens. Actuators B Chem.* **362**, 131765 (2022).
41. Geismar C, *et al.* Symptom profiles of community cases infected by influenza, RSV, rhinovirus, seasonal coronavirus, and SARS-CoV-2 variants of concern. *Sci. Rep.* **13**, 12511 (2023).
42. Xie D, *et al.* Engineered Switchable-Wettability Surfaces for Multi-Path Directional Transportation of Droplets and Subaqueous Bubbles. *Adv. Mater.* **35**, 2208645 (2023).
43. Long Z, *et al.* A Multi-Bioinspired Dual-Gradient Electrode for Microbubble Manipulation toward Controllable Water Splitting. *Adv. Mater.* **32**, 1908099 (2020).
44. Liu J, *et al.* An amplification-free digital droplet assay for influenza A viral RNA based on CRISPR/Cas13a. *Analyst* **150**, 1151-1157 (2025).
45. Rousogianni E, *et al.* Clinical features and outcomes of viral respiratory infections in adults during the 2023–2024 winter season. *Sci. Rep.* **15**, 35800 (2025).
46. Zhang X, *et al.* One-Step RAA and CRISPR-Cas13a Method for Detecting Influenza B Virus. *Microb. Biotechnol.* **18**, e70144 (2025).
47. Yang L, *et al.* A rapid and efficient platform for antiviral crRNA screening using CRISPR-Cas13a-based nucleic acid detection. *Front. Immunol.* **14**, 1116230 (2023).
48. Wang X, *et al.* A time-resolved luminescence assay using time-to-space conversion strategy for the sensitive detection of influenza virus on a microfluidic chip. *Biosens. Bioelectron.* **287**, 117679 (2025).
49. Ji J, *et al.* AM-DMF-ddRPA: an All-in-One Digital Microfluidic Platform for Rapid and Automatic Digital Nucleic Acid Analysis. *Angew. Chem. Int. Ed.* **64**, e202501913 (2025).

Acknowledgments: We acknowledge the critical support and infrastructure provided for this work by the Beijing Key Laboratory for Bioengineering and Sensing Technology. **Funding:** This work was supported by the funding from National Natural Science Foundation of China 22234001 (to Z.L.) and the National Key Research and Development Program of China 2023YFC2413001(to Z.L.).

Author contributions:

Conceptualization: Y.S. and Z.L.

Methodology: K.L., X.L., M.Z., Z.Y., J.W., J.L., H.Z., Y.Z. and Y.S.

Investigation: Y.S., Z.L., Y.Z. and K.L.

Visualization: K.L., X.L., Y.S., Z.L. and Y.Z.

Funding acquisition: Z.L.

Project administration: Y.S., Z.L., K.L. and X.L.

Supervision: Z.L. Writing—original draft: Y.S. and Z.L.

Writing—review and editing: K.L., X.L., Y.S. and Z.L.

Competing interests: The authors declare that they have no competing interests.

Data and materials availability: All data needed to evaluate the conclusions in the paper are present in the paper and/or the Supplementary Materials.

Supplementary Files

This is a list of supplementary files associated with this preprint. Click to download.

- MovieS1.mp4
- MovieS2.mp4
- MovieS3.mp4
- MovieS4.mp4
- MovieS5.mp4
- MovieS6.mp4
- MovieS7.mp4
- MovieS8.mp4
- SourceData.xlsx
- SupplementaryMaterials.docx
- NCOMMS26002870Tnrreportingsummary17684694221.pdf